

A Dual-Polarized 27-dBi Scanning Lens Phased Array Antenna for 5G Point-to-Point Communications

Zhang, Huasheng; Bosma, Sjoerd; Neto, Andrea; Llombart, Nuria

DOI

[10.1109/TAP.2021.3069494](https://doi.org/10.1109/TAP.2021.3069494)

Publication date

2021

Document Version

Final published version

Published in

IEEE Transactions on Antennas and Propagation

Citation (APA)

Zhang, H., Bosma, S., Neto, A., & Llombart, N. (2021). A Dual-Polarized 27-dBi Scanning Lens Phased Array Antenna for 5G Point-to-Point Communications. *IEEE Transactions on Antennas and Propagation*, 69(9), 5640-5652. Article 9395366. <https://doi.org/10.1109/TAP.2021.3069494>

Important note

To cite this publication, please use the final published version (if applicable). Please check the document version above.

Copyright

Other than for strictly personal use, it is not permitted to download, forward or distribute the text or part of it, without the consent of the author(s) and/or copyright holder(s), unless the work is under an open content license such as Creative Commons.

Takedown policy

Please contact us and provide details if you believe this document breaches copyrights. We will remove access to the work immediately and investigate your claim.

Green Open Access added to TU Delft Institutional Repository

'You share, we take care!' - Taverne project

<https://www.openaccess.nl/en/you-share-we-take-care>

Otherwise as indicated in the copyright section: the publisher is the copyright holder of this work and the author uses the Dutch legislation to make this work public.

A Dual-Polarized 27 dBi Scanning Lens Phased Array Antenna for 5G Point-to-Point Communications

Huasheng Zhang¹, Graduate Student Member, IEEE, Sjoerd Bosma², Graduate Student Member, IEEE, Andrea Neto³, Fellow, IEEE, and Nuria Llombart³, Fellow, IEEE

Abstract—A dual-polarized 4×4 scanning phased array antenna with leaky-wave enhanced lenses operating at 28 GHz is presented. Such an antenna can be used for point-to-point fifth-generation (5G) communications that require high gain, wide bandwidth (BW), and limited steering ranges. The proposed array has a periodicity of two wavelengths, and the resulting grating lobes are suppressed by directive and steerable array element patterns. To achieve a low-cost and low-profile solution, the leaky-wave antenna feeds are designed in printed circuit board and the lenses are made of plastic. The lenses are optimized in the near-field region of the feeds, with the goal of maximizing the array element aperture efficiency. The array performance obtained from the proposed approach is validated by full-wave simulations, showing a 27.5 dBi broadside gain at 28 GHz and a steering capability up to $\pm 20^\circ$ with 2 dB of scan loss. An antenna prototype was fabricated and measured. Measurement results are in excellent agreement with full-wave simulations. The prototype antenna, at broadside, achieves a 20% relative BW and a gain of 26.2 dBi.

Index Terms—Fifth generation (5G), leaky-wave antenna (LWA), lens antenna, millimeter wave, sparse phased array antenna (PAA).

I. INTRODUCTION

NEXT-generation wireless links between base stations and fixed access points, such as customer premise equipment (CPE) placed in a “smart home,” will operate at 28 GHz to exploit wide-bandwidth (BW) signals. To enable such links, it is necessary to have low-profile and low-cost antennas that support high gain and highly isolated dual polarization. Antenna alignment is of great importance to ensure proper connectivity in such links. Accordingly, the CPE antennas are required to support limited elevation beam steering, such as $\pm 10^\circ$ in all azimuthal directions. Table I shows the assumed requirements for the next generation of CPE millimeter-wave (mm-wave) antennas. To make the entire system compact

Manuscript received July 11, 2020; revised December 4, 2020; accepted December 31, 2020. Date of publication April 5, 2021; date of current version September 3, 2021. This work was partially supported by European Research Council Starting Grant, ERC-2014-StG LAA-THz-CC, under Grant 639749. (Corresponding author: Huasheng Zhang.)

The authors are with the THz Sensing Group, Microelectronics Department, Delft University of Technology, 2628 CD Delft, The Netherlands (e-mail: h.zhang-12@tudelft.nl; s.bosma@tudelft.nl; a.neto@tudelft.nl; n.llombartjuan@tudelft.nl).

Color versions of one or more figures in this article are available at <https://doi.org/10.1109/TAP.2021.3069494>.

Digital Object Identifier 10.1109/TAP.2021.3069494

0018-926X © 2021 IEEE. Personal use is permitted, but republication/redistribution requires IEEE permission. See <https://www.ieee.org/publications/rights/index.html> for more information.

TABLE I
ASSUMED REQUIREMENTS FOR 5G CPE ANTENNAS

Items	Requirements
Physical size	$\leq 10 \text{ cm} \times 10 \text{ cm} \times 2 \text{ cm}$
Array elements	4×4
Dual polarization	
Frequency band	26.5 – 29.5 GHz
Polarization isolation	$\geq 25 \text{ dB}$
Steering ability	$\pm 10^\circ$ in two main planes
Gain	27 dBi at broadside
Side lobe level	$\leq -10 \text{ dB}$
Scan loss	$\leq 2 \text{ dB}$

TABLE II
SIMULATED PERFORMANCE OF PAAs FOR
5G APPLICATIONS AT 28 GHz BAND

Ref.	Elements	Periodicity (λ_0 @ 28 GHz)	BW (GHz) (Single element)	Broadside Gain @ 28 GHz (dBi)	Pol. Isolation (dB)
[1]	1×4	1.1	27.1-29.5	16.3	\
[2]	4×4	0.56	23.5-30.5	19	\
[3]	1×16	0.56	25.6-29.8	20.2	\
[4]	8×8	0.55	26.8-29.9	21	20
[7]	8×8	0.59	27.5-32	22.4	18
This work	4×4	2	24.6-30.9	27.5	50

(*) Gains in italic are extracted from the simulated EIRP.

and low cost, the printed circuit board (PCB) technology is preferred to realize the antennas. An important challenge for these antennas is the desire for them to be compatible with inexpensive front ends that support 4×4 phase-shifted signals only while providing more than 27 dBi gain for broadside radiation and 25 dBi gain for steering cases. A sidelobe level (SLL) up to -10 dB can be accepted in communication links where the line of sight is dominating with respect to multipath effects.

Although great efforts have been dedicated to compact fifth-generation (5G) architectures in recent years, arrays with such performance have not been shown to date. In Table II, a summary of state-of-the-art 5G array antennas in PCB

is provided. In [1], a 1×4 dense-dielectric patch array antenna with a periodicity of $1.1\lambda_0$ (at 28 GHz) was proposed. It was designed with single polarization and achieved a relative BW of 8.5% and a gain of 16.3 dBi. To improve the performance on $\text{BW} \times \text{directivity}$, a 4×4 phased array antenna (PAA) with a smaller periodicity of $0.56\lambda_0$ was designed in [2], where single-polarized slots and patches were used. Such a structure achieved a relative BW of 26% and a gain of 19 dBi. With the same periodicity, in [3], a 1×16 PAA with single-polarized patches achieved a relative BW of 15.2% and a gain of 20.2 dBi. In [4], a higher gain of 21 dBi was achieved by using an 8×8 PAA with patches. This PAA has a lower relative BW of 11% [5]; however, it presents dual polarization with the polarization isolation better than 20 dB [6]. Recently, a better performance was reported in [7].

In this work, differently with respect to the antennas in Table II, we aimed at a much larger array periodicity of $2\lambda_0$, to reach 27 dBi gain with only 4×4 active elements, from 26.5 to 29.5 GHz. In the literature, sparse arrays in combination with partially reflecting layers have been proposed in [8] and [9] to suppress grating lobes and achieve high-gain steerable patterns with a small number of active elements. However, such arrays are characterized by narrow BW. In particular, only 5% relative BW was achieved for $2\lambda_0$ spacing in [10] and 10% when the periodicity is decreased to $1.5\lambda_0$ [8]. Such partially reflecting solutions would, therefore, not reach the required $\text{BW} \times \text{directivity}$ performance with just 16 active elements.

To achieve a wider BW, larger gain, and larger steering angles, we propose to use a scanning lens phased array architecture combined with leaky-wave antenna (LWA) feeds, which was introduced in the framework of the ERC grant LAA-THz-CC [11] and more recently in [12]. Small lenses phased arrays with limited steering ranges have been developed in mm-waves [13], as well as combining with focal plane arrays in one dimension to enlarge the steering range [14]. Here, the proposed antenna architecture consists of two components: a sparse PAA fabricated on a PCB and a movable dielectric (plastic) lens array, as shown in Fig. 1(a). Both arrays are arranged in a hexagonal grid with $2\lambda_0$ spacing at 28 GHz. The movable dielectric lens array, used as the add-on layer, ensures low grating lobe level (GLL) due to a highly directive and steerable array element pattern [12]. To illustrate the array concept, we can look to the radiation patterns in Fig. 1(c), with the reference system shown in Fig. 1(b). When the sparse PAA is steered to a certain angle (10°), the 16 array elements are electronically phase-shifted to steer the array factor to that angle (gray line). The grating lobes associated with this sparse array can be reduced by using a directive element pattern aligned to the same angle (red line). To achieve the dynamic steering of the directive element pattern, the lens array layer in Fig. 1(a) is mechanically translated with respect to the PAA along the x - or y -axis by a few millimeters. As a result, the array pattern, obtained as the product between the array element pattern and the array factor, shows a low GLL (blue line). To achieve such a low GLL over wide steering angles, array elements of high aperture efficiency are needed over the required frequency band and steering ranges [12].

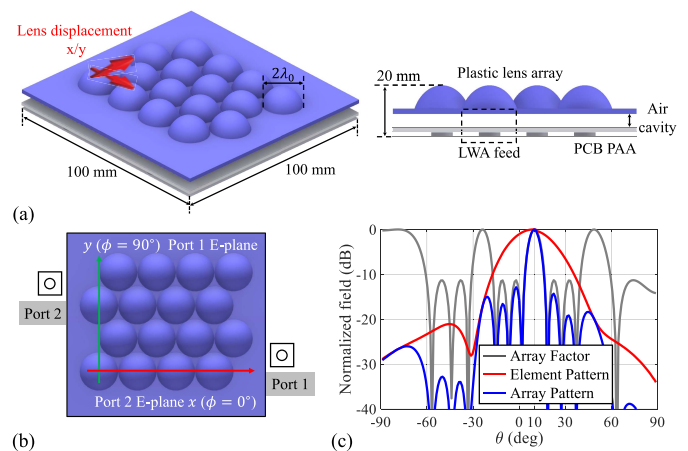


Fig. 1. (a) Perspective and side views of the proposed array antenna architecture, showing the movable plastic lens array, one of the LWA feeds in the sparse PCB PAA, and the air cavity that supports leaky waves. (b) Top view of the hexagonally arranged lens array together with the reference system used for radiation patterns. (c) Simulated array factor of the PCB PAA (port 1), array element pattern, and array pattern at 28 GHz along the E-plane ($\phi = 90^\circ$). The patterns are steered to 10° in the E-plane, and the lens array is displaced by 2.4 mm in the same direction. PAA: phased array antenna. LWA: leaky-wave antenna.

In the proposed array antenna, each radiating element is a leaky-wave (Fabry-Pérot) antenna [15], [16]. It illuminates the corresponding lens through a $\lambda_0/2$ air cavity [see Fig. 1(a)], where a couple of TE/TM leaky-wave modes are excited. These modes attenuate fast because of the low contrast between the air and the plastic layer, and thereby, they do not reach to the next array element. This type of feed is particularly efficient in illuminating the top portion of dielectric lenses [16]. Moreover, the proposed antenna is capable to steer a dual-polarized beam. The two independent ports shown in Fig. 1(b) can be used for transmitting two independent signals. In [12], the proposed array, operating at submillimeter wavelengths, is based on silicon lenses excited by leaky-wave waveguide feeds. In this work, the lens array concept is adapted to the technology requirements for 5G communications. In particular, the lens array is made of high-density polyethylene (HDPE), with $\epsilon_r = 2.34$ and $\tan \delta = 0.0003$. This type of plastic is low cost, low loss, and suitable for milling technique used for mass production [17]. Moreover, the proposed dual-polarized LWA feeds based on this low-contrast material will achieve a wide BW [17]. Simulations show a 22.7% BW from 24.6 to 30.9 GHz, with the polarization isolation better than 50 dB over the entire BW.

Once such an array architecture is selected, one of the biggest technological challenges is that the required performance should be guaranteed with a maximum volume occupation of $10 \text{ cm} \times 10 \text{ cm} \times 2 \text{ cm}$. The proposed scanning lens PAA is, in principle, scalable with periodicity. However, the maximum vertical dimension leads to a lens diameter of $2\lambda_0$. These electrically small lenses are not usually analyzed using standard physical optics (PO) techniques. For instance, in [14], full-wave simulations are proposed as a mean of optimization. Moreover, the lenses are in the near-field region of the LWA feeds. Consequently, we adopt the

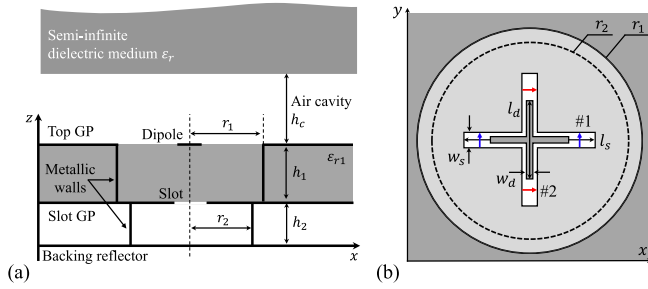


Fig. 2. Proposed resonant LWA feed. (a) Lateral view. A resonant air cavity with the height of $h_c = \lambda_0/2$ is placed below a semi-infinite dielectric medium illuminated by slot-fed dipoles. (b) Top view of the crossed dipoles (w_d, l_d) fed by crossed slots (w_s, l_s). Each slot is fed in balance by two discrete ports that are placed symmetrically at the arms of the slot. The upper and lower metal cavities are circular with the radius of r_1 and r_2 , respectively. GP: ground plane.

techniques developed in [18] and [19] for optimizing such lenses in reception combining geometrical optics (GO) and Fourier optics (FO) approaches. The agreement between the radiation patterns of the 4×4 array antenna obtained using the proposed techniques and full-wave simulations is excellent for both broadside and steering cases. Moreover, the simulated broadside gain is above 26.8 dBi from 26.5 to 29.5 GHz and reaches 27.5 dBi at 28 GHz. The array antenna is also capable of steering toward 20° in all planes with 2 dB scan loss. To validate the antenna design, the PCB PAA was fabricated with fixed phase shifts among array elements implemented in corporate feeding networks. Three separate PCBs were fabricated to validate the electrical steering performance of the proposed antenna in three static steering conditions: broadside and 10° steering in the two main planes. The measured prototype showed a -10 dB matching BW of 20% from 25.1 to 30.7 GHz, a gain of 26.2 dBi at broadside, and a scan loss less than 2 dB.

This article is organized as follows. Section II introduces the design criteria for the resonant LWA feed. Section III describes the methodology for the near-field lens design and the validation of the proposed approach. Section IV describes the PCB design for the proposed antenna. Section V shows the fabricated antenna prototype and the corresponding measurement results.

II. DUAL-POLARIZED LWA FEED

The lenses are fed by resonant dual-polarized LWAs, as shown in Fig. 2. The antenna consists of coupled slot-fed dipoles surrounded by resonant metal cavities. The proposed geometry is similar to the one used in [10] but operates over a much wider BW, from 24 to 30.5 GHz. Moreover, the LWA feed here supports dual polarization. The main criteria for the LWA feed design and the simulated performance of the optimized structure are discussed in the following.

A. Dual-Polarized Slot-Fed Dipole Configuration

In a standard LWA, there are a couple of nearly degenerated TE_1/TM_1 leaky waves propagating radially with multiple reflections, leaking at the same time energy into the infinite

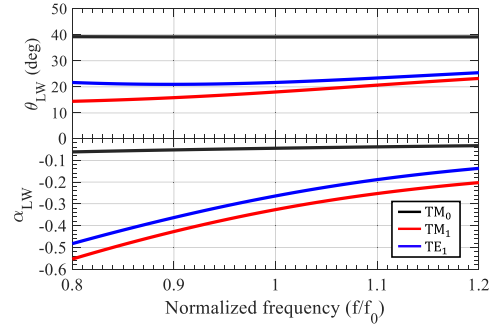


Fig. 3. Solutions of the dispersion equation, $k_{LW} = k_0 \sqrt{\epsilon_r} (\sin \theta_{LW} + j \alpha_{LW})$, for the stratification shown in Fig. 2(a), where $h_c = \lambda_0/2$ and $\epsilon_r = 2.34$. The top y-axis shows the radiation angle θ_{LW} of each leaky-wave mode, whereas the bottom axis presents the attenuation constant α_{LW} .

air medium [15]. This effect enlarges the effective area of the antenna with a compromise on BW [20]. To enhance the $BW \times$ directivity performance, a resonant LWA radiating into a semi-infinite dense medium, as shown in Fig. 2(a), was proposed in [16]. In this article, wide frequency BW in the order of 20% is targeted. Accordingly, the medium should have a low relative permittivity [17].

The radiation properties of the LWA feed shown in Fig. 2 are determined by the solutions of the dispersion equation, $k_{LW} = k_0 \sqrt{\epsilon_r} (\sin \theta_{LW} + j \alpha_{LW})$, where k_{LW} is the propagation constant of a leaky-wave mode, k_0 is the propagation constant in free space, θ_{LW} is the radiation angle of the leaky-wave mode, and α_{LW} is the attenuation constant. θ_{LW} and α_{LW} for the main leaky-wave modes are shown in Fig. 3. It can be seen that for an HDPE lens, the main TE_1/TM_1 leaky-wave modes point toward $\theta_{LW} \approx 20^\circ$ and form a single and symmetric beam around broadside since $\sin \theta_{LW} \approx |\alpha_{LW}|$ [21]. Moreover, there is also an undesired TM_0 mode propagating [22], which radiates toward 40° in the E-plane of the feed. In [17], it was shown that this mode can be exploited to increase the lens aperture efficiency. However, this is not the case for the electrically small lenses in the current configuration since the effective area associated with this mode is larger than the lens diameter. Therefore, the excitation of this mode must be reduced, for example, by using a double-slot iris feed [22]. Here, to facilitate the dual-polarized feed design, a slot-fed dipole configuration [see Fig. 2(b)] is used, similar to what was done in [10].

The dual polarization is realized by using crossed dipoles fed by crossed slots, each one dedicated to a different polarization, as shown in Fig. 2(b). The dipole oriented along the y-axis is fed by the slot 1, while the other orthogonal dipole is coupled to slot 2. In [23], each of the crossed slot is fed in balance by two offset feeding lines placed symmetrically at the arms of the slot. By doing so, the level of the current induced on the other unfed slot will be very low, and thus, higher isolation between the two slots (or polarizations) will be achieved. Moreover, it can facilitate impedance matching, as discussed in [24]. Here, to simplify the simulation of the proposed structure, each slot is excited by two discrete ports at their arms coherently, as shown in Fig. 2(b). In Section IV, this

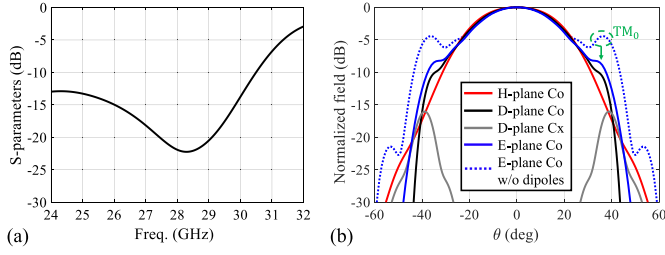


Fig. 4. Simulated performance of the LWA feed (slot 1) shown in Fig. 2 when radiating into a semi-infinite HDPE medium ($\epsilon_r = 2.34$). (a) S-parameters. (b) FF. In the E-plane ($\phi = 90^\circ$), the patterns with and without (w/o) the use of dipoles are shown. Cx: cross polarization. FF: far field.

structure will be adapted and optimized for PCB fabrication, and the discrete ports will be replaced by microstrip lines.

B. Resonant Metal Cavities

In the vertical stratification shown in Fig. 2(a), there are three metallic layers separated by dielectric and air layers of thickness h_1 and h_2 , respectively. In order to avoid the excitation of higher order surface waves in these layers, h_1 and h_2 are chosen to be less than half wavelength. With this condition, only the TM_0 surface wave mode can propagate in each of these layers. To suppress this mode, circular metallic walls placed surrounding the slots and the dipoles are used [see Fig. 2(b)]. The dimensions of the walls (radius $r_{1/2}$) are designed in such a way that most of the surface waves reflected from the walls can cancel out the outgoing surface waves excited by the slots, as discussed in [25].

C. Simulated Performance

The structure in Fig. 2 is symmetric, and thus, the performance of only one polarization (slot 1) was optimized to have the widest BW and the lowest TM_0 leaky-wave mode. The optimized dimensions of the LWA feed are: $w_d = 0.2$ mm, $l_d = 2.87$ mm, $w_s = 0.34$ mm, $l_s = 5.49$ mm, $r_1 = 4.12$ mm, $r_2 = 3.64$ mm, $\epsilon_{r1} = 3.66$, $h_1 = 1.59$ mm, and $h_2 = 1.63$ mm. The simulated matching and far-field performance of the LWA feed when radiating in the semi-infinite HDPE ($\epsilon_r = 2.34$) medium are shown in Fig. 4(a) and (b), respectively. As it can be seen in Fig. 4(a), the -10 dB band is from 24 to 30.5 GHz. The coupling between the two polarizations is below -90 dB and is not reported here. In Fig. 4(b), it is clearly shown that the TM_0 leaky-wave mode along the E-plane ($\phi = 90^\circ$) is well suppressed when the dipole is introduced and optimized, i.e., from the blue dotted curve to the blue solid curve.

III. NEAR-FIELD LENS DESIGN

The main driver for the optimization of the lens shape is the maximization of its aperture efficiency since it directly impacts the level of grating lobes [12]. Therefore, we used elliptical lenses [17], [26] with eccentricity $e = 1/\sqrt{\epsilon_r}$ ($\epsilon_r = 2.34$), truncation angle θ_0 seen from the lower focus of the lens [see Fig. 5(a)], and a fixed diameter of $D_{lens} = 2\lambda_0$.

To optimize the aperture efficiency of a single lens antenna, the analysis is performed in reception following the GOFO approach described in [19]. In this approach, the power

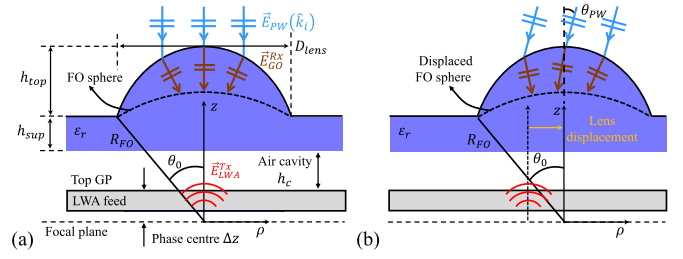


Fig. 5. Geometry of the elliptical HDPE ($\epsilon_r = 2.34$) lens illuminated by the LWA feed in Fig. 2. The FO scenario is depicted when the lens is (a) aligned and (b) displaced along the ρ axis with respect to the feed. The optimized lens dimensions are: $D_{lens} = 2\lambda_0$ (at 28 GHz), $\theta_0 = 33.5^\circ$, $R_{FO} = 1.81\lambda_0$, $\Delta z = 0.81\lambda_0$, $h_{top} = 0.85\lambda_0$, $h_{sup} = 0.2\lambda_0$, $h_c = \lambda_0/2$.

received by the LWA feed is evaluated as the field correlation between the GO fields, \vec{E}_{GO}^{Rx} and \vec{H}_{GO}^{Rx} , generated by an incident plane wave propagating along \hat{k}_i , and the field radiated by the LWA feed, \vec{E}_{LWA}^{Tx} and \vec{H}_{LWA}^{Tx} , over an equivalent sphere centered at the lower focus of the lens [FO sphere in Fig. 5(a)] as follows:

$$\begin{aligned}
 P_L(\hat{k}_i) &= \frac{1}{16P_{rad}^{LWA}} \\
 &\times \left| \int_0^{2\pi} \int_0^{\theta_0} \left(\frac{1}{\zeta} \vec{E}_{GO}^{Rx}(\hat{k}_i) \cdot \vec{E}_{LWA}^{Tx} - \zeta \vec{H}_{GO}^{Rx}(\hat{k}_i) \cdot \vec{H}_{LWA}^{Tx} \right) \right. \\
 &\quad \left. \times R_{FO}^2 \sin\theta d\theta d\phi \right|^2 \quad (1)
 \end{aligned}$$

where ζ is the characteristic impedance of the lens medium, R_{FO} is the radius of the FO sphere, and P_{rad}^{LWA} is the total power radiated by the LWA inside the lens. The aperture efficiency of this lens antenna, η_{ap} , can be obtained by normalizing the received power, P_L , by the power of incident plane wave, $P_{inc} = 0.5|\vec{E}_{PW}|^2 A_{lens}/\zeta_0$, where $|\vec{E}_{PW}|$ is the amplitude of the plane wave, $A_{lens} = \pi D_{lens}^2/4$ is the projected area of the lens surface, and ζ_0 is the free-space impedance. The GO fields, \vec{E}_{GO}^{Rx} and \vec{H}_{GO}^{Rx} , are obtained following the procedures explained in [19], even though the validity of the GO approach is questionable for such small lenses. The fields radiated by the LWA feed on the FO sphere, \vec{E}_{LWA}^{Tx} and \vec{H}_{LWA}^{Tx} , cannot be evaluated using the far-field approximation since the FO sphere is too close to the feed. Instead, the near fields are calculated using the spectral Green's function, where the equivalent magnetic currents on the top of the ground plane are taken as a source. These currents have been exported from a full-wave simulation of the LWA feed in the presence of the semi-infinite dielectric medium [see Fig. 2(a)] using CST [27]. It is worth mentioning that although the FO sphere is close to the feed, the field on the FO sphere can still be considered as a local spherical wave, and therefore, (1) can be simplified for the on-focus feed as a field matching between the electric fields, \vec{E}_{GO}^{Rx} and \vec{E}_{LWA}^{Tx} only, as described in [17].

A. Array Element Performance

The lens dimensions were optimized in the near field for one polarization (slot 1) at broadside. The optimization procedure

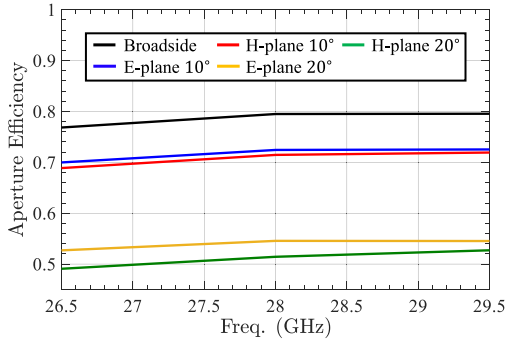


Fig. 6. Aperture efficiency of the optimized lens illuminated by the LWA feed shown in Fig. 2, for the cases of broadside, steering toward $\theta = 10^\circ$ and 20° in the E- and H-planes.

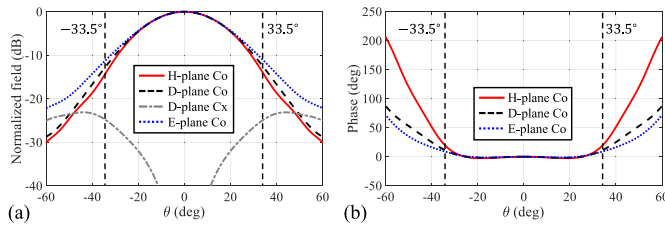


Fig. 7. Near field radiated by the LWA feed in Fig. 2 (slot 1) at 28 GHz and at broadside on the FO sphere. (a) Amplitude. (b) Phase. The near field is plotted along the FO sphere with the radius of $R_{FO} = 1.81\lambda_0$. The lens geometry is optimized and its truncation angle is 33.5° .

is as follows. First, the far fields (FFs) of the feed in a semi-infinite dielectric medium are calculated [see Fig. 4(b)], from which the phase center is extracted. For an LWA feed, it is known that its phase center is located below the ground plane [28]. The phase center is then aligned with the lower focus of the lens. Second, the far-field patterns are used to calculate an initial estimate of the lens dimensions (a , b , θ_0) geometrically, by imposing $D_{lens} = 2\lambda_0$. Finally, the broadside aperture efficiency is optimized iteratively by evaluating the near field, \vec{E}_{LWA}^{Tx} , and then performing the field matching over the corresponding FO sphere increasing or decreasing the lens truncation angle θ_0 and the phase center location. The optimized truncation angle is 33.5° , the total height of the lens is $1.05\lambda_0$ (11.25 mm), and the phase center is $0.81\lambda_0$ (8.68 mm) below the top ground plane. The resulting aperture efficiency is shown as a function of frequency in Fig. 6. As it can be seen, the broadside aperture efficiency is above 75% over the entire frequency band.

The broadside near field over the FO sphere radiated at 28 GHz is shown in Fig. 7 in co- and cross-polarizations according to Ludwig's third definition. Indeed, the amplitude of the near field differs significantly from the one in the FF [see Fig. 4(b)]. There is better field symmetry in ϕ up to the truncation angle and lower cross-polarization level.

In the steering cases, the lens should be displaced along the ρ -axis with respect to the feed by a few millimeters to steer the element pattern of the array. To calculate the steering performance of the array elements and evaluate the optimal lens displacement, the field radiated by the feed, \vec{E}_{LWA}^{Tx} , should

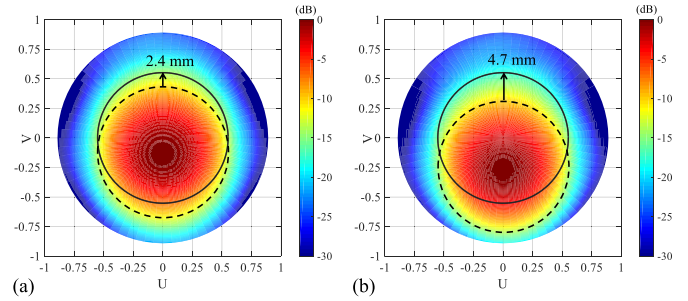


Fig. 8. Near fields radiated by the LWA feed (slot 1) at 28 GHz on the FO spheres for the displaced lenses, seen from the coordinate system in Fig. 5(b). Lenses are displaced by (a) 2.4 and (b) 4.7 mm along the E-plane ($\phi = 90^\circ$), corresponding to $\theta = 10^\circ$ and 20° steering, respectively. The dashed and black solid circles represent the aligned and displaced FO spheres (with respect to the feed), respectively.

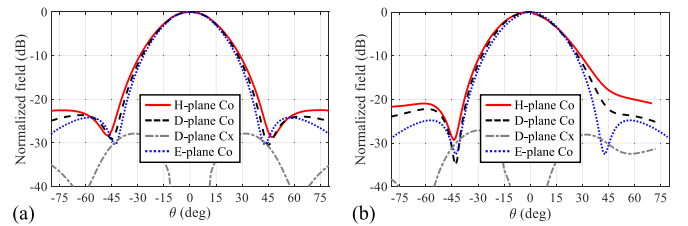


Fig. 9. Array element patterns when the lens is (a) aligned with respect to the LWA feed and (b) displaced by 2.4 mm along the H-plane ($\phi = 0^\circ$), steering to $\theta = 10^\circ$. Note that the pattern in (b) points toward 10° in H-plane when the reference system is aligned to that of (a). The reference system used in (b) is instead aligned toward the maximum direction of radiation.

be calculated over the displaced FO sphere [see Fig. 5(b)]. The aperture efficiency can then be calculated in the same way as the broadside case. Note that in this case, the reference system is still at the lens focus, but the FO sphere is not spherical seen from the feed position. The steering analysis is performed for steering angles of 10° and 20° in the main planes. These angles correspond to lens displacement of 2.4 and 4.7 mm along the steering directions, respectively. The amplitude of the fields over the FO sphere in these two steering cases is shown in Fig. 8, where the dashed and solid black circles represent the aligned and displaced FO spheres (with respect to the feed), respectively. It is clear that larger displacement leads to larger spillover loss. Furthermore, for larger displacement, the angle between \vec{E}_{LWA}^{Tx} and the lens-air interface can reach the critical angle [17], leading to reduced reflection efficiency. The aperture efficiency, shown in Fig. 6, is above 70% for 10° steering and above 50% for 20° steering.

The element pattern of the array can be evaluated using (1) by varying the incident angle, θ_{PW} in Fig. 5(b), and the polarization of the incident plane wave [19]. The array element pattern when the lens is aligned to the feed is shown in Fig. 9(a). This broadside pattern is almost symmetric in ϕ and has a cross-polarization level below -25 dB. The array element pattern when steering in the H-plane ($\phi = 0^\circ$) to $\theta = 10^\circ$ is shown in Fig. 9(b). The steering is achieved by displacing the lens 2.4 mm in the positive x -axis, and the steered pattern still shows good symmetry and high directivity.

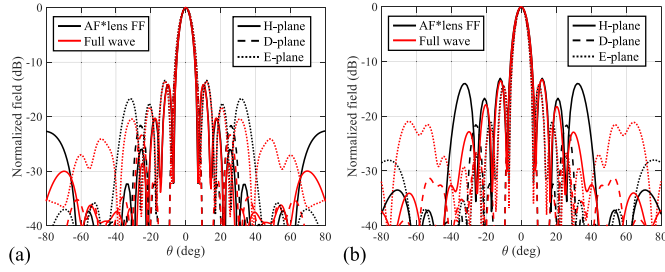


Fig. 10. Broadside co-pol FFs radiated by the proposed scanning lens PAA at 28 GHz fed by (a) port 1 (slots 1) and (b) port 2 (slots 2). The black curves represent the FFs calculated by using the GOFO approach. The red curves show the CST full-wave simulations. The reference system used for the patterns is shown in Fig. 1(b).

B. Array Performance

The lens array consists of 16 lenses with $D_{lens} = 2\lambda_0$ arranged in four rows in which the uneven rows are shifted by λ_0 to form a regular triangular grid [see Fig. 1(b)]. The PAA has the same configuration with the $2\lambda_0$ periodicity, illuminating the lens array through the $\lambda_0/2$ air cavity. This hexagonal configuration is adopted since it can achieve a lower SLL with respect to a rectangular configuration. The array pattern, steered to (θ_s, ϕ_s) , is obtained as the product between the array element pattern (see Fig. 9) and the array factor $AF(\theta_s, \phi_s)$. The grating lobes in the array factor that arise from the sparse array sampling are suppressed by the directive array element pattern [12], which is shown in Fig. 1(c).

Three radiation cases are discussed in this section: broadside and steering to 10° and 20° in E- and H-planes, respectively. The broadside radiation patterns of the proposed scanning lens PAA, fed by ports 1 and 2 at 28 GHz, are shown by the black curves in Fig. 10(a) and (b), respectively. Here, port 1 represents the case when all slots 1 [see Fig. 2(b)] are excited simultaneously, whereas port 2 corresponds to exciting slots 2. The first sidelobe is below -13 dB for both cases. A high directivity of 28 dBi is obtained with only 16 elements due to the presence of the lenses. Moreover, the grating lobes from the array factor are significantly suppressed by the directive array element pattern shown in Fig. 9(a). The radiation patterns of the array obtained with the GOFO approach have been verified using the full-wave solver of CST. The simulated patterns are shown by the red curves in Fig. 10 for both ports. It can be seen that there is an excellent agreement between the CST simulation and the GOFO approach for the main lobe and the first few sidelobes. Wider angles are not accurately modeled by the GOFO approach since the edge effect of the array and the spillover from one lens to the next is not considered in this approach.

In the steering cases, the lens array is displaced by 2.4 and 4.7 mm toward the steering directions, i.e., 10° and 20° in H- and E-planes, respectively. The steered radiation patterns of the array, fed by port 1 at 28 GHz, are shown in Fig. 11 and compared to full-wave simulations. The H-plane ($\phi = 0^\circ$) steering is shown in Fig. 11(a) for 10° and 20° , whereas the E-plane ($\phi = 90^\circ$) steering is shown in Fig. 11(b). Moreover, the simulated patterns in UV-plane are shown in Fig. 11(c) and (d), for the cases of H- and E-plane steering

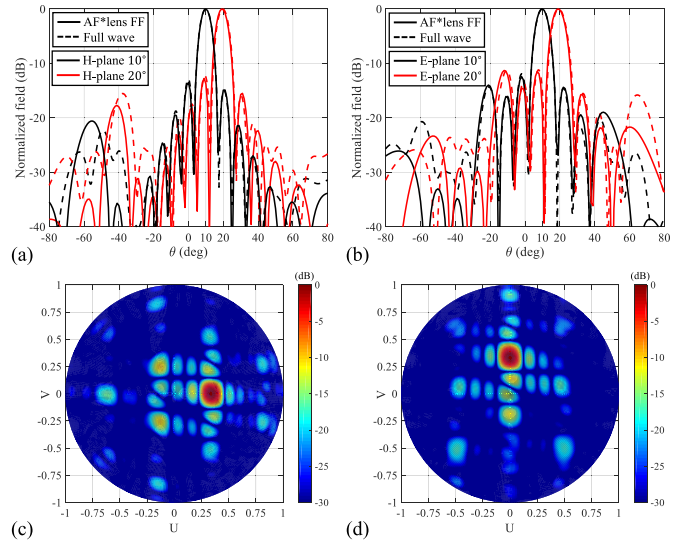


Fig. 11. Co-pol FFs radiated by the proposed scanning lens PAA at 28 GHz fed by port 1 (slots 1) at (a) H-plane ($\phi = 0^\circ$) and (b) E-plane ($\phi = 90^\circ$) when steering toward 10° (black) and 20° (red). The solid and dashed lines represent the GOFO approach and the CST full-wave simulations, respectively. (c) and (d) Full-wave results of (a) and (b) when steering to 20° in the UV-plane, respectively. The reference system used for the patterns is shown in Fig. 1(b). The lens array is displaced by 2.4 and 4.7 mm toward the steering directions for 10° and 20° steering cases, respectively.

to 20° , respectively. In Fig. 11(a) and (b), the patterns evaluated using the GOFO approach (solid lines) show excellent agreement with the full-wave simulations (dashed lines) for the main lobes and the first few sidelobes. Moreover, the SLLs evaluated using the GOFO approach are below -10 dB for both steering angles and both ports. It is worth mentioning that the proposed approach is quite efficient. The calculation of the array patterns is orders of magnitude faster than the full-wave simulations (approximately 4.5 h for CST versus a couple of minutes for the GOFO method).

The simulated array active S-parameters for port 1 (slots 1) for all radiation cases are shown in Fig. 12. As it can be seen, the matching performance is very good within the required frequency band, even for 20° steering cases. Since the feeds are far away from each other, the mutual coupling between the feeds is always lower than -20 dB.

Finally, the simulated directivity of the array is shown as a function of frequency in Fig. 13 for both ports. The broadside directivity is 28 dBi at 28 GHz and above 27.3 dBi in the designed BW. For the cases of steering, the scan loss is below 1 and 2 dB in the whole band when steering to 10° and 20° , respectively. The directivity evaluated using the GOFO approach is overall 0.3–0.8 dB lower than the CST simulations, depending on frequencies and steering angles. This is related to the aforementioned pattern differences at the larger elevation angles ($\theta \geq 40^\circ$). However, the accuracy of the far-field performance is good enough for design purposes.

IV. PCB ANTENNA DESIGN

The LWA feed shown in Fig. 2 is the simplified geometry used for analyzing and optimizing the performance of an array element. In this section, this geometry is optimized for

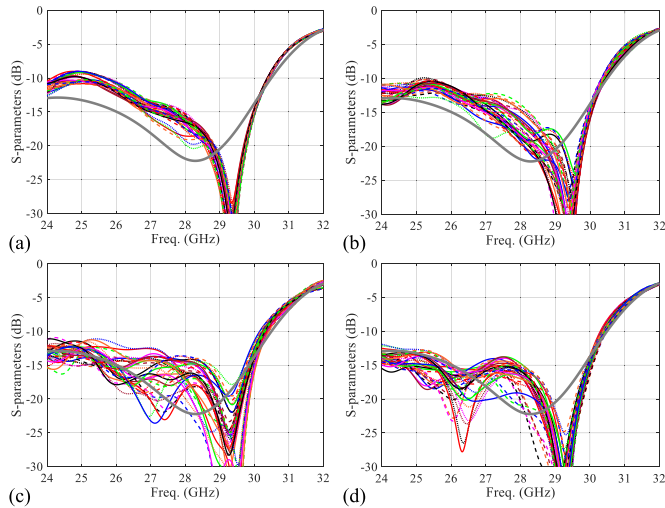


Fig. 12. Simulated array active S-parameters for port 1 (slots 1) for the cases of (a) broadside, (b) steering to 10° in H-plane ($\phi = 0^\circ$), (c) 20° in H-plane, and (d) 20° in E-plane ($\phi = 90^\circ$). The lens array is displaced by 2.4 and 4.7 mm for the steering cases. The gray thick line is the S-parameter for the single LWA feed [see Fig. 4(a)].

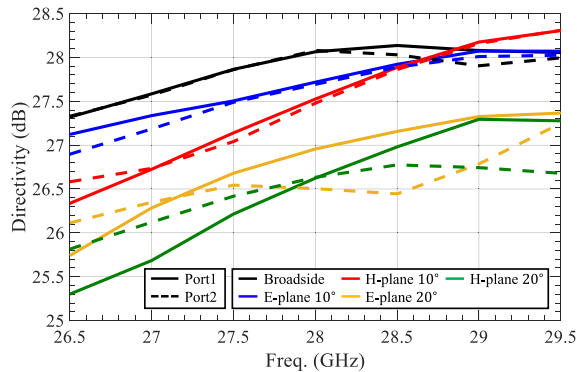


Fig. 13. Simulated directivity of the 16-element array for port 1 (solid lines) and port 2 (dashed lines), for broadside, 10° , and 20° steering in both E- and H-planes. The array is displaced by 2.4 and 4.7 mm for the steering cases.

the implementation in PCB technology, including the proper feeding topology. The proposed PCB design presents excellent radiation efficiency ($>97\%$) and no back radiation in a relative BW of 22.7%. Moreover, corporate feeding networks with fixed phase shifts between array elements are designed to validate the proposed antenna architecture in predefined and static steering conditions.

A. Optimized LWA Feed in PCB

Referring back to Fig. 2, the LWA feed consists of three metal layers and one dielectric layer. The dual polarization is realized by exciting symmetrically the crossed slots at their arms with discrete ports. In a PCB design, the stratification consists of multiple layers and the slots are excited by microstrip lines. The main challenge comes from the feeding design for the crossed slots in PCB. In [23], each of the crossed slots is fed symmetrically by a set of dual-offset microstrip lines that are connected to the input port through a reactive power combiner. However, since the two sets of microstrip

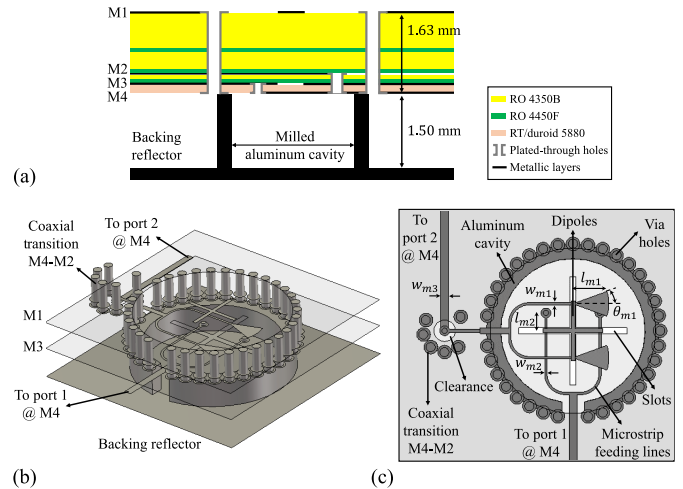


Fig. 14. PCB dual-polarized LWA feed. (a) PCB stratification. (b) Perspective and (c) top views of the detailed antenna structure. The slots are excited in balance by two sets of microstrip lines, each one dedicated to a different polarization. The lines with radial open stubs (w_{m1} , l_{m1} , and θ_{m1}) are at M2, while the ones with short stubs (w_{m2} and l_{m2}) are at M4. The optimized dimensions of this antenna are: $\epsilon_{r1} = 3.66$, $w_{m1} = w_{m2} = 0.12$ mm, $w_{m3} = 0.38$ mm, $l_{m1} = 1.66$ mm, $\theta_{m1} = 40^\circ$, $l_{m2} = 0.88$ mm, $w_s = 0.32$ mm, $l_s = 5.31$ mm, $w_d = 0.2$ mm, $l_d = 2.95$ mm, $h_1 = 1.63$ mm, $r_1 = 4.28$ mm, $h_2 = 1.5$ mm, and $r_2 = 3.55$ mm.

lines are designed on the same dielectric layer, an air bridge is used to avoid intersection between the microstrip lines. To achieve good performance and practical implementation with standard PCB technology at 5G frequencies, the two sets of dual-offset microstrip lines are placed instead at the opposite sides of the ground plane, similar to what was done in [29].

The optimized PCB stratification is shown in Fig. 14(a), combined with the externally milled backing reflector. The PCB substrates are Rogers material, with the relative permittivity of 3.66, 3.52, and 2.2 for RO 4350B, RO 4450F, and RT/duroid 5880, respectively. There are four metal layers, M1–M4, in the PCB. M1 is the top ground plane where the crossed dipoles are printed, M3 is the slot ground plane, and M2 and M4 are layers for microstrip feeding lines. The upper circular metallic wall between the slot plane and the top ground plane shown in Fig. 2(a) is made of plated-through via holes within the PCB from M1 to M4 [see Fig. 14(a)], with a height of 1.63 mm and a radius of 4.28 mm. While the lower metal wall is realized by a continuous milled aluminum cavity between the PCB and the backing reflector, with a height of 1.5 mm and a radius of 3.55 mm. Both cavities are fine-tuned for the best impedance matching and suppression of surface waves. The perspective and top views of the detailed antenna structure are shown in Fig. 14(b) and (c), respectively. Visible in the figures are two rings of metallization realized by via holes and aluminum cavity. In the top view, the crossed slot-fed dipoles are shown. Each slot is fed coherently by two offset microstrip lines that are combined together by a reactive power combiner located at the opposite sides (M2/M4) of the slot ground plane (M3). Specifically, the microstrip lines on M2 are designed with radial open stubs, while the ones on M4 are short stubs made of via holes. The short-stub design

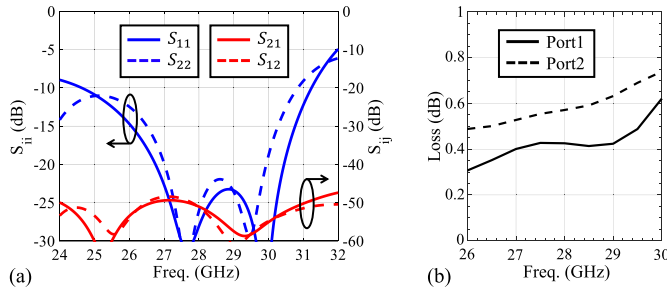


Fig. 15. Simulated performance of the dual-polarized PCB LWA feed when radiating in the semi-infinite HDPE medium. (a) S-parameters. Note that the ohmic and dielectric losses are not included in the simulation. (b) Total loss of the feed, including the excitation of surface waves, ohmic, and dielectric losses (dielectric loss in the HDPE medium is not included here).

is commonly used since it makes the design more compact. However, in our case, the two stubs on M2 and M4 cannot be designed symmetrically using both short stubs because there would be intersection between via holes and microstrip lines. Although the asymmetric stub design introduces complexity, a wideband impedance matching is best achieved using the dimension described in Fig. 14(c).

In the final array design, we will use corporate feeding networks located at the bottom layer M4 to excite all array elements. Therefore, the microstrip lines on M4 are directly connected to the port 1 via the feeding network that will be described in Section IV-B. On the contrary, the microstrip lines on M2 need vertical transitions from M4 to M2 to connect to port 2 through the feeding network. Such a transition structure is made by emulating a coaxial using via holes from M4 to M2 [30], as shown in Fig. 14. This coaxial transition can significantly alter the matching performance of the feed because of the limited fabrication tolerances in standard PCB technology. To make the design more robust, we have shortened the height of the via holes and enlarged the clearance on M3 [see Fig. 14(c)] as much as possible. The optimized matching performance of the proposed coaxial transition shows a wideband behavior ($S_{11} < -25$ dB) over the entire frequency band.

The matching performance of the entire PCB LWA feed is simulated and reported in Fig. 15(a). Here, the antenna radiates in the semi-infinite HDPE medium. The -10 dB band is from 24.6 to 30.9 GHz, i.e., 22.7% relative BW. Moreover, the mutual coupling between the ports is very low, which is in the order of -50 dB. The total loss of the feeding antenna, including the excitation of surface waves, ohmic, and dielectric losses, is reported in Fig. 15(b) for both ports. As it can be seen, the total loss is less than 0.6 and 0.8 dB for port 1 and port 2 up to 30 GHz, respectively. The loss in port 2 is a bit larger due to the coaxial transition structure. For the far-field performance, it is very close to the one in Fig. 4(b).

B. Feeding Network

To validate the array architecture discussed in Section III-B, all 16 dual-polarized LWA feeds (in Fig. 14) are connected by two specific corporate feeding networks fed by two ports, one per polarization, as shown in Fig. 16. The feeding networks

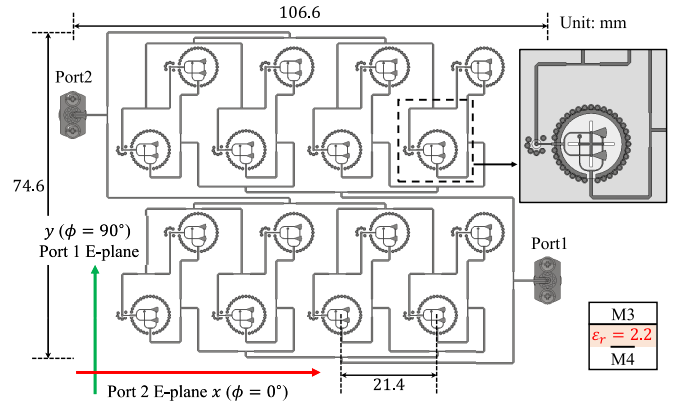


Fig. 16. PCB feeding networks located at the bottom layer M4 used for broadside radiation. Note that some components such as dipoles are not shown here. The reference system for two ports is also shown. The top inset shows one of the array elements, which is the same as the one in Fig. 14(c). Here, all components are shown. The bottom inset shows the lateral structure for the feeding networks.

are done using microstrip lines fabricated on an RT/duroid 5880 layer and are located at the M4 layer of the proposed stratification in Fig. 14(a). The lengths of the microstrip lines are designed to guarantee uniform amplitude excitation and appropriate progressive phase shifts between array elements that would lead to the desired steering angles. Each array element is excited by the two ports through four power dividers (see Fig. 16). The short stubs on M4 are connected to port 1 directly through the feeding network, while the opening stubs on M2 are first connected to M4 through the coaxial transition structures and then excited by port 2 through the feeding network.

To demonstrate the capability of the array to electronically steer toward broadside and $\pm 10^\circ$ in the two main planes, three separate PCBs were designed and fabricated with fixed progressive phase shifts between array elements. The performance of such feeding networks in all three PCBs was simulated, showing impedance matching below -23 dB over the whole frequency band and an ohmic loss of approximately 1.6 dB. The power division, $1 \rightarrow 1/16$, is simulated to guarantee a maximum deviation of 1.4 dB among all array elements. The expected progressive phase shifts as a function of frequency also show very little dispersion, with the phase deviating from ideal linear phase shifts by less than 5° over the entire band.

V. ANTENNA PROTOTYPE AND MEASUREMENT

We have fabricated and measured a prototype to validate the proposed antenna architecture. The prototype consists of three parts: an HDPE lens array, three different PCBs, and a milled aluminum cavity, which are manufactured separately and then assembled together. As mentioned before, the three PCBs are fabricated with different feeding networks where the fixed phase shifting conditions are implemented, in order to validate the steering capability of the antenna toward broadside, $\theta = 10^\circ$ and $\phi = 0^\circ$, and $\theta = 10^\circ$ and $\phi = 90^\circ$. The mechanical displacement of the lens array was implemented only for these three steering conditions, by introducing a fixed

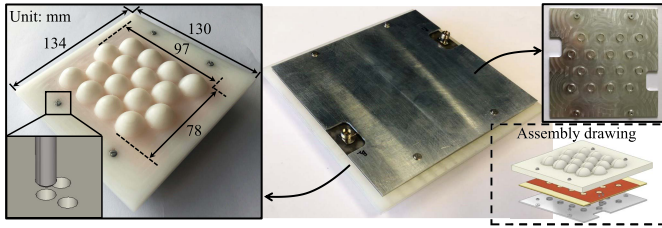


Fig. 17. Photographs of the assembled antenna prototype. The milled HDPE elliptical lens array is shown on the left side, where the inset shows the screw holes used for the displacement of the lens layer. Right: perspective view of the antenna. The milled aluminum cavity and the assembly drawing are shown in the top and bottom insets, respectively.

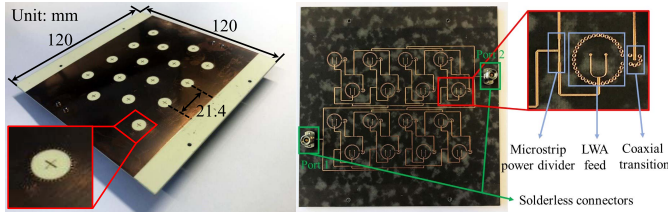


Fig. 18. Photographs of the fabricated PCB used for broadside radiation. The top metal layer M1 is shown on the left side, where the inset shows the crossed dipoles. Right: bottom view of the PCB and the feeding networks are shown. Inset: one of the feeding elements in the PAA.

displacement of the lens layer of 0 and 2.4 mm in the two main planes, respectively.

The fabricated antenna prototype is shown in Fig. 17. As it can be seen in the assembly drawing on the right side, the different parts of the prototype are aligned with screws. The milled aluminum cavity is shown on the top right side and the milled lens array is shown on the left, where the inset shows three screw holes with a spacing of 2.4 mm. These holes are used to displace and align the lens layer with respect to the PCBs used for the three steering directions. It is worth mentioning that the dimension of the radiating aperture associated with the lens array is 97 mm \times 78 mm, while the fabricated prototype has an area of 130 mm \times 134 mm. The outer extra rim was included to facilitate the fabrication in the workshop.

The PCB for broadside radiation is shown in Fig. 18. The top layer M1 is shown on the left, with the crossed dipoles shown in the inset. Moreover, the bottom feeding networks on M4 are shown on the right. One of the 16 feeding elements is in the inset, with the coaxial transition, and fed through the feeding networks by two connectors that are at the corners of the PCB. It can be seen that the PCB size is 120 mm \times 120 mm instead of 100 mm \times 100 mm. The extra rim was included to facilitate the alignment with the lens array.

A. S-Parameter Characterization

The loss in microstrip lines is estimated using a TRL calibration kit, which is around 0.27 dB/cm at 28 GHz. This loss is higher than the one obtained using a simple surface impedance model. At higher frequencies, the effects of metal roughness and surface finish have been pointed as causes for this higher line loss [31].

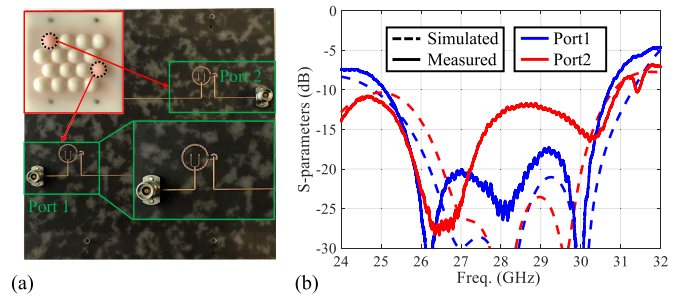


Fig. 19. Two HDPE lenses illuminated by two LWA feeds that are excited directly by two ports, each one dedicated to a different polarization. (a) Photograph of the PCB. (b) Measured S-parameters compared to simulations.

The matching performance for both polarizations of a single lens antenna was measured using a different PCB showing in Fig. 19(a). Two marked lenses in the lens array are illuminated by two LWA feeds that are directly excited by two ports, each one dedicated to a different polarization. The measured S-parameters are shown in Fig. 19(b) and compared to simulations (all losses are included). As it can be seen, the -10 dB band of port 1 is from 25.1 to 30.7 GHz, i.e., 20% relative BW, whereas for port 2, the BW is wider, but the reflection coefficient is higher (-12 dB) around the central frequency. This can be related to the limited tolerances of the fabricated PCBs, especially due to the close location of the vias in the upper cavity with respect to the microstrip lines [see Fig. 14(c)]. This tolerance problem is not present in port 1. Therefore, the matching performance of port 1 is much better than that of port 2. The matching performance of the arrays with different steering configurations was also measured. The reflection coefficients are below -10 dB over the whole band for all steering cases.

B. Far-Field Performance

The far-field patterns, directivity, and gain of the array antenna were measured in an anechoic chamber. These properties were reconstructed from a near-field planar scanning measurement done in front of the lens array.

The reference system for the far-field radiation patterns is the same as the one in Fig. 1(b). The measured co-pol patterns of both ports at 28 GHz, compared to simulations, are shown in Fig. 20 for the cases of broadside, steering to $\theta = 10^\circ$ and $\phi = 0^\circ$, and $\theta = 10^\circ$ and $\phi = 90^\circ$, respectively. Moreover, the co-pol patterns at 26.5 and 29.5 GHz for the two steering cases are shown in Fig. 21. In the steering cases, the lens array is displaced by 2.4 mm toward the positive x - and y -directions, respectively. In the figures, the co-pol patterns along $\phi = 0^\circ$ and/or $\phi = 90^\circ$ planes are plotted. The cross-pol patterns are below -20 dB at all frequency points and are not shown here. As it can be seen from Figs. 20 and 21, the agreement between simulations and measurements is excellent for all radiation cases. Moreover, the steered beams accurately point toward 10° in both main planes. In Figs. 20(f) and 21(c), the SLL is a bit higher (-8.5 dB) due to fabrication tolerances, but for other radiation cases, the SLLs are below -10 dB. The measured 2-D far-field patterns of port 1 at 28 GHz are shown in Fig. 22

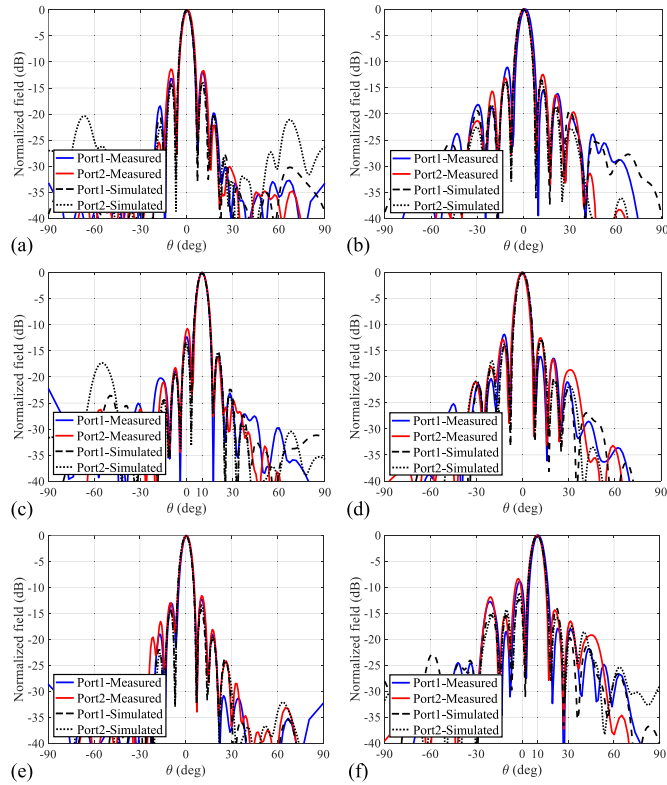


Fig. 20. Measured far-field co-pol radiation patterns at 28 GHz when steering to (a) and (b) broadside, (c) and (d) $\theta = 10^\circ$ and $\phi = 0^\circ$, and (e) and (f) $\theta = 10^\circ$ and $\phi = 90^\circ$. The first column shows the FFs at $\phi = 0^\circ$ plane, whereas the second column shows $\phi = 90^\circ$ plane. The reference system is defined in Fig. 1(b). The lens array is displaced by 2.4 mm toward the steering directions for the steering cases.

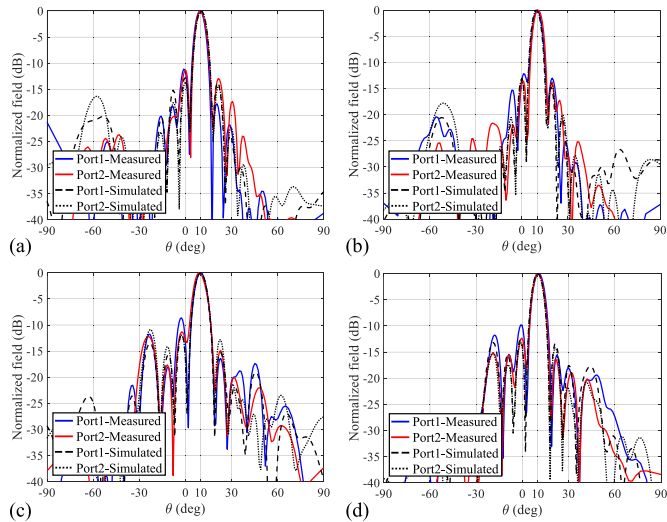


Fig. 21. Measured far-field co-pol radiation patterns when steering to $\theta = 10^\circ$ and $\phi = 0^\circ$ at (a) 26.5 and (b) 29.5 GHz and to $\theta = 10^\circ$ and $\phi = 90^\circ$ at (c) 26.5 and (d) 29.5 GHz. The reference system is defined in Fig. 1(b). The lens array is displaced by 2.4 mm toward the steering directions.

for broadside and steering cases. In the figures, the position of sidelobes and the cross-pol values are clearly shown.

The measured broadside and steering directivity and gain, as a function of frequency, are shown in Fig. 23 and compared to simulations. In the case of directivity, i.e., in

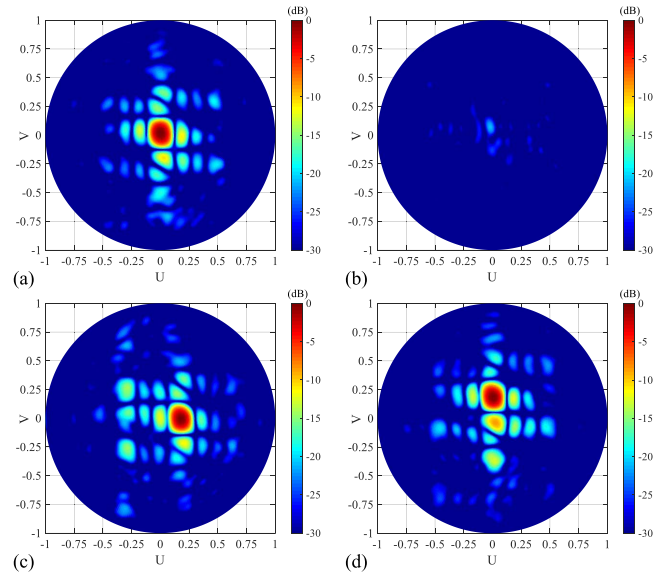


Fig. 22. Measured 2-D far-field radiation patterns of port 1 at 28 GHz. (a) Broadside co-pol pattern. (b) Cross-pol pattern. Co-pol patterns when steering to (c) $\theta = 10^\circ$ and $\phi = 0^\circ$ and (d) $\theta = 10^\circ$ and $\phi = 90^\circ$. The reference system is defined in Fig. 1(b). The lens array is displaced by 2.4 mm toward the steering direction for the steering cases.

Fig. 23(a), (c), and (e), the measurements are in very good agreement with the simulations for the cases of broadside and steering to $\theta = 10^\circ$ and $\phi = 0^\circ$ and for both ports. When steering to $\theta = 10^\circ$ and $\phi = 90^\circ$, port 2 performs worse than port 1, especially at 28.5 GHz. By exploring the measured near fields, it was observed that up to two lenses in the array were not illuminated, which explains the drop of 1 dB in directivity when compared to port 1. This issue is associated with the limited fabrication tolerances, especially in the PCB vias, as mentioned before in Section V-A. However, the capability of steering toward $\theta = 10^\circ$ and $\phi = 90^\circ$ is validated by port 1.

The calibrated gains for all radiation cases are shown in Fig. 23(b), (d), and (f). In the figures, the simulated broadside gain is above 26.8 dBi over the required frequency band and reaches 27.5 dBi at 28 GHz. Moreover, the scan loss is less than 1 dB when steering to 10° . For the measured gain, the losses in feeding networks (around 3.5 dB) and connectors (around 0.2 dB) are calibrated out. As it can be seen, the calibrated gain of both ports fluctuates significantly in broadside case, while less in steering cases. This is possibly associated with the multiple reflections in the measurement setup. For port 1, the agreement is quite good. The broadside gain is above 26.2 dBi and the steering gain is above 26 dBi over the required frequency band. Port 2 performs worse: the gain is above 25.2 dBi at broadside, 25.6 dBi when steering to $\theta = 10^\circ$ and $\phi = 0^\circ$, and 24 dBi when steering to $\theta = 10^\circ$ and $\phi = 90^\circ$. The gain of port 2 in Fig. 23(f) is 2 dB less than that of port 1 because of the previously mentioned tolerance (adding 1 dB lost in the feeding network). It is worth mentioning that the measurement of the gain (via the near-field power evaluation instead of a far-field calibrated link) can have some inaccuracy due to the multiple reflections. Moreover,

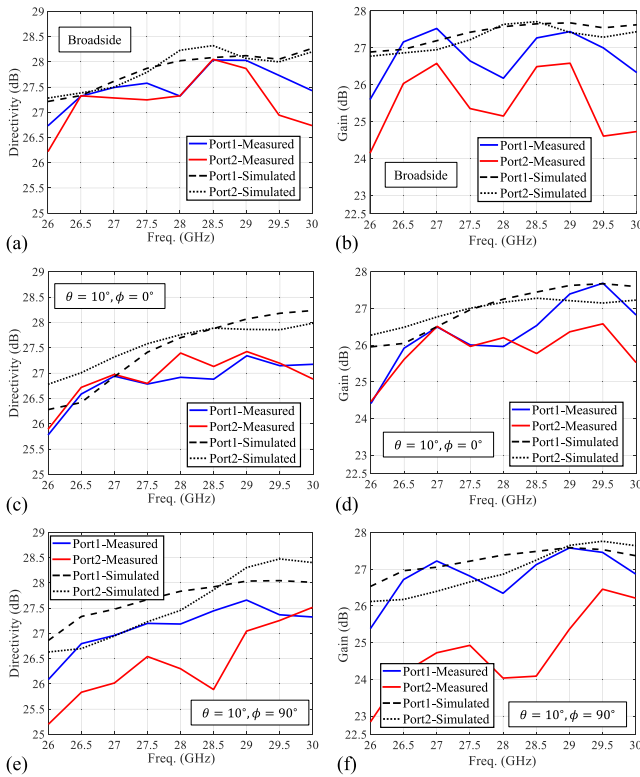


Fig. 23. Measured directivity at (a) broadside, (c) $\theta = 10^\circ$ and $\phi = 0^\circ$, and (e) $\theta = 10^\circ$ and $\phi = 90^\circ$; Calibrated gain at (b) broadside, (d) $\theta = 10^\circ$ and $\phi = 0^\circ$, and (f) $\theta = 10^\circ$ and $\phi = 90^\circ$. The lens array is displaced by 2.4 mm toward the steering direction for the steering cases.

the estimation of the losses in the feeding networks is done by considering a microstrip line with uniform impedance and a length approximately the same as the actual implemented networks.

To conclude, the measured far-field properties are overall in very good agreement with the simulations. Although port 2 performs a bit worse than port 1, the proposed antenna architecture is well validated. To further improve the prototype performance, the PCBs, lens array, and metal cavity should undergo a fine fabrication tuning cycle.

VI. CONCLUSION

A hexagonally arranged sparse scanning lens PAA, with two-wavelength spacing, has been proposed and demonstrated to provide 27 dBi gain over the frequency band from 26.5 to 29.5 GHz, with just 16 active feeding elements. The grating lobes caused by the array sparsity can be reduced by designing a directive array element pattern. When the PAA steers toward an angle, the lens array will be displaced, in order to steer simultaneously the element pattern toward the same angle, thus achieving also low GLL while steering.

The challenges of the design emerge due to the simultaneous requirements of high efficiency over broadband while also implementing dual polarization. To meet these challenges while maintaining a low-cost structure, a dual-polarized LWA feed in PCB was co-designed with plastic elliptical lenses. It achieves a wide relative BW of 22.7%, from 24.6 to

30.9 GHz, and a polarization isolation better than 50 dB. It is worth mentioning that the analysis of lenses with diameters of only two wavelengths would have been a challenge even in the absence of the other challenges. We implemented an analysis in reception, using the near-field evaluation of the LWA feed in an infinite medium in combination with the GOFO approach for the elliptical lens. The optimized lens antenna shows above 75% and 70% aperture efficiency for broadside and 10° steering over the required band, respectively. The array performance obtained from the proposed GOFO approach was validated by CST full-wave simulations for both polarizations and all steering cases. It is shown that the broadside gain is larger than 26.8 dBi and can reach 27.5 dBi at 28 GHz, with SLL lower than -13 dB. Moreover, the design procedure is well validated even for steering up to 20° , with a scan loss lower than 2 dB.

The proposed array antenna was fabricated and measured, and the measurement validated the proposed antenna architecture. The array can achieve 26.2 dBi gain at broadside and 26 dBi gain when steering to 10° , with a 20% relative BW, from 25.1 to 30.7 GHz. If a better fabrication tuning cycle is made, the performance could be improved further. Moreover, the proposed array antenna can be easily expanded into more elements, such as 8×8 within $20 \text{ cm} \times 20 \text{ cm} \times 2 \text{ cm}$. A gain around 33.5 dBi would be achieved. Although in the current prototype the feeding networks and the lens mechanical displacement are fixed, a phased array with electrical steering capability can be achieved by using the proposed antenna architecture. The array elements can be fed by low-cost active chips to achieve continuous electrical steering, and the lens array can be displaced continuously by using low-cost and low-power piezomotors [32].

ACKNOWLEDGMENT

The authors would like to thank Ulrik Imberg, Huawei, Sweden, for useful discussions during the development of this antenna prototype. The antenna prototype was developed under a contract with Huawei Technologies, Sweden AB. The lens array architecture and modeling tool were developed in the framework of the ERC.

REFERENCES

- [1] O. M. Haraz, A. Elboushi, S. A. Alshebeili, and A.-R. Sebak, "Dense dielectric patch array antenna with improved radiation characteristics using EBG ground structure and dielectric superstrate for future 5G cellular networks," *IEEE Access*, vol. 2, pp. 909–913, 2014.
- [2] C.-X. Mao, S. Gao, and Y. Wang, "Broadband high-gain beam-scanning antenna array for millimeter-wave applications," *IEEE Trans. Antennas Propag.*, vol. 65, no. 9, pp. 4864–4868, Sep. 2017.
- [3] M. Khalily, R. Tafazolli, P. Xiao, and A. A. Kishk, "Broadband mm-wave microstrip array antenna with improved radiation characteristics for different 5G applications," *IEEE Trans. Antennas Propag.*, vol. 66, no. 9, pp. 4641–4647, Sep. 2018.
- [4] X. Gu *et al.*, "Development, implementation, and characterization of a 64-element dual-polarized phased-array antenna module for 28-GHz high-speed data communications," *IEEE Trans. Microw. Theory Techn.*, vol. 67, no. 7, pp. 2975–2984, Jul. 2019.
- [5] X. Gu *et al.*, "A multilayer organic package with 64 dual-polarized antennas for 28 GHz 5G communication," in *IEEE MTT-S Int. Microw. Symp. Dig.*, Honolulu, HI, USA, Jun. 2017, pp. 1899–1901.

- [6] D. Liu, X. Gu, C. W. Baks, and A. Valdes-Garcia, "Antenna-in-package design considerations for Ka-band 5G communication applications," *IEEE Trans. Antennas Propag.*, vol. 65, no. 12, pp. 6372–6379, Dec. 2017.
- [7] A. Nafe, M. Sayginer, K. Kibaroglu, and G. M. Rebeiz, " 2×64 -element dual-polarized dual-beam single-aperture 28-GHz phased array with 2×30 Gb/s links for 5G polarization MIMO," *IEEE Trans. Microw. Theory Techn.*, vol. 68, no. 9, pp. 3872–3884, Sep. 2020.
- [8] D. Blanco, N. Llombart, and E. Rajo-Iglesias, "On the use of leaky wave phased arrays for the reduction of the grating lobe level," *IEEE Trans. Antennas Propag.*, vol. 62, no. 4, pp. 1789–1795, Apr. 2014.
- [9] F. Scattone, M. Ettore, B. Fuchs, R. Sauleau, and N. J. G. Fonseca, "Synthesis procedure for thinned leaky-wave-based arrays with reduced number of elements," *IEEE Trans. Antennas Propag.*, vol. 64, no. 2, pp. 582–590, Feb. 2016.
- [10] D. Blanco, E. Rajo-Iglesias, A. M. Benito, and N. Llombart, "Leaky-wave thinned phased array in PCB technology for telecommunication applications," *IEEE Trans. Antennas Propag.*, vol. 64, no. 10, pp. 4288–4296, Oct. 2016.
- [11] *European Research Council Starting Grant (ERC-2014-StG LAA-THz-CC)*, Delft Univ. Technol., Delft, The Netherlands, Oct. 2015. [Online]. Available: <https://cordis.europa.eu/project/id/639749/reporting>.
- [12] M. Alonso-Delpino, S. Bosma, C. Jung-Kubiak, G. Chattopadhyay, and N. Llombart, "Wideband multimode leaky-wave feed for scanning lens-phased array at submillimeter wavelengths," *IEEE Trans. THz Sci. Technol.*, vol. 11, no. 2, pp. 205–217, Mar. 2021.
- [13] J. C. R. Poirier, G. A. Morin, Y. M. M. Antar, and J. W. Moffat, "Millimetre-wave limited-scan array using small lenses," in *Proc. IEEE Antennas Propag. Soc. Int. Symp.*, Boston, MA, USA, vol. 2, Jul. 2001, pp. 823–826.
- [14] G. Mumcu, M. Kacar, and J. Mendoza, "Mm-wave beam steering antenna with reduced hardware complexity using lens antenna subarrays," *IEEE Antennas Wireless Propag. Lett.*, vol. 17, no. 9, pp. 1603–1607, Sep. 2018.
- [15] D. R. Jackson, A. A. Oliner, and A. Ip, "Leaky-wave propagation and radiation for a narrow-beam multiple-layer dielectric structure," *IEEE Trans. Antennas Propag.*, vol. 41, no. 3, pp. 344–348, Mar. 1993.
- [16] N. Llombart, G. Chattopadhyay, A. Skalare, and I. Mehdi, "Novel terahertz antenna based on a silicon lens fed by a leaky wave enhanced waveguide," *IEEE Trans. Antennas Propag.*, vol. 59, no. 6, pp. 2160–2168, Jun. 2011.
- [17] M. A. Campo, D. Blanco, S. Bruni, A. Neto, and N. Llombart, "On the use of fly's eye lenses with leaky-wave feeds for wideband communications," *IEEE Trans. Antennas Propag.*, vol. 68, no. 4, pp. 2480–2493, Apr. 2020.
- [18] S. Bosma, H. Zhang, A. Neto, and N. Llombart, "A dual-polarized 27 dBi scanning lens phased array antenna for 5G point-to-point communications," in *Proc. Eur. Conf. Antennas Propag. (EuCAP)*, Copenhagen, Denmark, 2020.
- [19] H. Zhang, S. O. Dabironezare, G. Carluccio, A. Neto, and N. Llombart, "A Fourier optics tool to derive the plane wave spectrum of quasi-optical systems [EM programmer's notebook]," *IEEE Antennas Propag. Mag.*, vol. 63, no. 1, pp. 103–116, Feb. 2021.
- [20] A. Neto, N. Llombart, G. Gerini, M. D. Bonnedal, and P. de Maagt, "EBG enhanced feeds for the improvement of the aperture efficiency of reflector antennas," *IEEE Trans. Antennas Propag.*, vol. 55, no. 8, pp. 2185–2193, Aug. 2007.
- [21] G. Lovat, P. Burghignoli, and D. R. Jackson, "Fundamental properties and optimization of broadside radiation from uniform leaky-wave antennas," *IEEE Trans. Antennas Propag.*, vol. 54, no. 5, pp. 1442–1452, May 2006.
- [22] N. Llombart, A. Neto, G. Gerini, M. Bonnedal, and P. De Maagt, "Impact of mutual coupling in leaky wave enhanced imaging arrays," *IEEE Trans. Antennas Propag.*, vol. 56, no. 4, pp. 1201–1206, Apr. 2008.
- [23] C. H. Tsao, Y. M. Hwang, F. Kilburg, and F. Dietrich, "Aperture-coupled patch antennas with wide-bandwidth and dual-polarization capabilities," in *Proc. IEEE AP-S Int. Symp., Antennas Propag.*, Syracuse, NY, USA, vol. 3, Jun. 1988, pp. 936–939.
- [24] S. D. Targonski, R. B. Waterhouse, and D. M. Pozar, "Design of wide-band aperture-stacked patch microstrip antennas," *IEEE Trans. Antennas Propag.*, vol. 46, no. 9, pp. 1245–1251, Sep. 1998.
- [25] A. Neto, N. Llombart, G. Gerini, and P. DeMaagt, "On the optimal radiation bandwidth of printed slot antennas surrounded by EBGs," *IEEE Trans. Antennas Propag.*, vol. 54, no. 4, pp. 1074–1083, Apr. 2006.
- [26] D. F. Filipovic, S. S. Gearhart, and G. M. Rebeiz, "Double-slot antennas on extended hemispherical and elliptical silicon dielectric lenses," *IEEE Trans. Microw. Theory Techn.*, vol. 41, no. 10, pp. 1738–1749, Oct. 1993.
- [27] *CST Microwave Studio*. Accessed: 2020. [Online]. Available: <http://www.cst.com>
- [28] P. Burghignoli, "A leaky-wave analysis of the phase center in Fabry-Pérot cavity antennas," *IEEE Trans. Antennas Propag.*, vol. 60, no. 5, pp. 2226–2233, May 2012.
- [29] M. Yamazaki, M. Haneishi, and E. T. Rahardjo, "Construction of a slot-coupled planar antenna for dual polarisation," *Electron. Lett.*, vol. 30, no. 22, pp. 1814–1815, Oct. 1994.
- [30] W. H. Syed, D. Cavallo, H. T. Shivamurthy, and A. Neto, "Wide-band, wide-scan planar array of connected slots loaded with artificial dielectric superstrates," *IEEE Trans. Antennas Propag.*, vol. 64, no. 2, pp. 543–553, Feb. 2016.
- [31] A. Deutsch, C. W. Surovic, R. S. Krabbenhoft, G. V. Kopsay, and B. J. Chamberlin, "Prediction of losses caused by roughness of metalization in printed-circuit boards," *IEEE Trans. Adv. Packag.*, vol. 30, no. 2, pp. 279–287, May 2007.
- [32] M. Alonso-Delpino, C. Jung-Kubiak, T. Reck, N. Llombart, and G. Chattopadhyay, "Beam scanning of silicon lens antennas using integrated piezomotors at submillimeter wavelengths," *IEEE Trans. THz Sci. Technol.*, vol. 9, no. 1, pp. 47–54, Jan. 2019.



Huasheng Zhang (Graduate Student Member, IEEE) received the B.Eng. degree (*cum laude*) in electronic information engineering from Beihang University, Beijing, China, in 2016, and the M.Sc. degree (*cum laude*) in electrical engineering from the Delft University of Technology (TU Delft), Delft, The Netherlands, in 2018, where he is currently pursuing the Ph.D. degree with the Terahertz Sensing Group.

His research interests include the design of quasi-optical systems and antenna feeds for next-generation communication and sensing systems.



Sjoerd Bosma (Graduate Student Member, IEEE) received the B.Sc. and M.Sc. (*cum laude*) degrees in electrical engineering from the Delft University of Technology (TU Delft), Delft, The Netherlands, in 2015 and 2017, respectively, where he is currently pursuing the Ph.D. degree with the Terahertz Sensing Group, with a focus on leaky-wave lens antenna arrays.

From September 2018 to February 2019, he participated in the JPL Visiting Student Researcher Program at the Jet Propulsion Laboratory, Pasadena, CA, USA.



Andrea Neto (Fellow, IEEE) received the Laurea degree (*summa cum laude*) in electronic engineering from the University of Florence, Florence, Italy, in 1994, and the Ph.D. degree in electromagnetics from the University of Siena, Siena, Italy, in 2000. Part of his Ph.D. degree was developed at the European Space Agency Research and Technology Center, Noordwijk, The Netherlands.

He worked for the Antenna Section at the European Space Agency Research and Technology Center for over two years. From 2000 to 2001, he was a Post-Doctoral Researcher with the California Institute of Technology, Pasadena, CA, USA, where he worked at the Sub-mm Wave Advanced Technology Group. From 2002 to January 2010, he was a Senior Antenna Scientist with TNO Defence, Security, and Safety, The Hague, The Netherlands. In February 2010, he became a Full Professor of applied electromagnetism at the Department of Electrical Engineering, Mathematics and Computer Science, Delft University of Technology, Delft, The Netherlands, where he formed and leads the THz Sensing Group. His research interests include the analysis and design of antennas with an emphasis on arrays, dielectric lens antennas, wideband antennas, EBG structures, and THz antennas.

Dr. Neto is a member of the Technical Board of the European School of Antennas and an organizer of the course on antenna imaging techniques. He is also a member of the Steering Committee of the Network of Excellence NEW-FOCUS, dedicated to focusing techniques in millimeter and sub-millimeter wave regimes. He was a recipient of the European Research Council Starting Grant to perform research on advanced antenna architectures for THz sensing systems in 2011, the H. A. Wheeler Award for the best applications paper of 2008 in the IEEE TRANSACTIONS ON ANTENNAS AND PROPAGATION, the Best Innovative Paper Prize of the 30th ESA Antenna Workshop in 2008, and the Best Antenna Theory Paper Prize of the European Conference on Antennas and Propagation (EuCAP) in 2010. He served as an Associate Editor for the IEEE TRANSACTIONS ON ANTENNAS AND PROPAGATION from 2008 to 2013 and IEEE ANTENNAS AND WIRELESS PROPAGATION LETTERS from 2005 to 2013.



Nuria Llombart (Fellow, IEEE) received the master's degree in electrical engineering and the Ph.D. degree from the Polytechnic University of Valencia, Valencia, Spain, in 2002 and 2006, respectively.

During her master's degree studies, she spent one year at the Friedrich-Alexander University of Erlangen-Nuremberg, Erlangen, Germany, and worked at the Fraunhofer Institute for Integrated Circuits, Erlangen, Germany. From 2002 to 2007, she was with the Antenna Group, TNO Defense, Security and Safety Institute, The Hague, The Netherlands, working as a Ph.D. student and afterward as a Researcher. From 2007 to 2010, she was a Post-Doctoral Fellow with the California Institute of Technology, Pasadena, CA, USA, working with the Submillimeter Wave Advance Technology Group, Jet Propulsion Laboratory, Pasadena. She was a "Ramón y Cajal" Fellow with the Department of Optics, Complutense University of Madrid, Madrid, Spain, from 2010 to 2012. In September 2012, she joined the THz Sensing Group, Delft University of Technology, Delft, The Netherlands, where she has been a Full Professor since February 2018. She has coauthored more than 150 journal and international conference contributions. Her research interests include the analysis and design of planar antennas, periodic structures, reflector antennas, lens antennas, and waveguide structures, with an emphasis on the THz range.

Dr. Llombart was a recipient H. A. Wheeler Award for the Best Applications Paper of 2008 in the IEEE TRANSACTIONS ON ANTENNAS AND PROPAGATION, the 2014 THz Science and Technology Best Paper Award of the IEEE Microwave Theory and Techniques Society, the 2014 IEEE Antenna and Propagation Society Lot Shafai Mid-Career Distinguished Achievement Award, the European Research Council Starting Grant in 2015, and several NASA awards. She serves as a Board Member for the IRMMW-THz International Society.